

# Active contours driven by local Gaussian distribution fitting energy

Li Wang<sup>a</sup>, Lei He<sup>b</sup>, Arabinda Mishra<sup>c,\*</sup>, Chunming Li<sup>c</sup>

<sup>a</sup> School of Computer Science and Technology, Nanjing University of Science and Technology, Nanjing 210094, China

<sup>b</sup> Information Technology Department, Armstrong Atlantic State University, Savannah, GA 31419, USA

<sup>c</sup> Institute of Imaging Science, Vanderbilt University, Nashville, TN 37232-2310, USA

## ARTICLE INFO

### Article history:

Received 31 August 2008

Received in revised form

3 February 2009

Accepted 13 March 2009

Available online 21 March 2009

### Keywords:

Image segmentation

Intensity inhomogeneity

Active contour model

Probability distribution

Level set method

Variational method

## ABSTRACT

This paper presents a new region-based active contour model in a variational level set formulation for image segmentation. In our model, the local image intensities are described by Gaussian distributions with different means and variances. We define a local Gaussian distribution fitting energy with a level set function and local means and variances as variables. The energy minimization is achieved by an interleaved level set evolution and estimation of local intensity means and variances in an iterative process. The means and variances of local intensities are considered as spatially varying functions to handle intensity inhomogeneities and noise of spatially varying strength (e.g. multiplicative noise). In addition, our model is able to distinguish regions with similar intensity means but different variances. This is demonstrated by applying our method on noisy and texture images in which the texture patterns of different regions can be distinguished from the local intensity variance. Comparative experiments show the advantages of the proposed method.

© 2009 Elsevier B.V. All rights reserved.

## 1. Introduction

Image segmentation is a fundamental task in many image processing and computer vision applications. Due to the presence of noise, low contrast, and intensity inhomogeneity, it is still a difficult problem in majority of applications. In particular, intensity inhomogeneity is a significant challenge to classical segmentation techniques such as edge detection and thresholding.

Image segmentation in general has been studied extensively in the past decades. A well-established class of methods are active contour models, which have been widely used in image segmentation with promising results. The models can achieve subpixel accuracy and provide closed and smooth contours/surfaces. The existing active contour models can be broadly categorized into two classes: edge-based models [1–7] and region-based

models [8–18]. A good review of major active contour models can be found in Refs. [19–21].

Edge-based models utilize image gradient to guide curve evolution, which are usually sensitive to noise and weak edges [11]. Instead of utilizing image gradient, region-based models typically aim to identify each region of interest by using a certain region descriptor, such as intensity, color, texture or motion, to guide the motion of the contour [20]. Therefore region-based models generally have better performance in the presence of image noise and weak object boundaries. In addition, region-based models are less sensitive to the initial contour locations than edge-based models.

Region-based models [8–11,13–15] tend to rely on global information to guide contour evolution. For example, the well-known piecewise constant (PC) models are based on the assumption that image intensities are statistically homogeneous in each region, and thus fail to segment the images with intensity inhomogeneity. For segmentation of more general images, two similar active contour models [14,12] were proposed under the

\* Corresponding author.

E-mail address: [arabinda.mishra@vanderbilt.edu](mailto:arabinda.mishra@vanderbilt.edu) (A. Mishra).

framework of minimization of the Mumford–Shah functional [22]. These models, widely known as piecewise smooth (PS) models, can handle intensity inhomogeneity to some extent. The computational cost of the PS models is, however, rather expensive due to the complicated procedures involved [16,23].

In practice, intensity inhomogeneity occurs in many real-world images acquired with different modalities [23]. In particular, it is often seen in medical images, such as microscopy, computer tomography (CT), ultrasound, and magnetic resonance imaging (MRI). For example, the intensity inhomogeneity in MRI often appears as an intensity variation across the image, due to radio frequency (RF) coils or acquisition sequences. Thus the resultant intensities of the same tissue vary with the locations in the image. Similar artifacts also occur in CT images due to the beam hardening effect, as well as in ultrasound images caused by non-uniform beam attenuation within the body. In addition, images are often corrupted by various noises that challenge the segmentation [24].

Recently, local intensity information has been incorporated into the active contour models [25,16,23,26,27] for more accurate segmentation, especially in the presence of intensity inhomogeneity. For example, Li et al. [25,23] proposed a local binary fitting (LBF) energy in a region-based model for more accurate and efficient segmentation. The LBF model draws upon local intensity means, which enables it to cope with intensity inhomogeneity. With local intensity information, the LBF model is able to recover object boundaries accurately. In [28,29], both local intensity means and variances are used to characterize the local intensity distribution in their proposed active contour models. However, the local intensity means and variances are defined empirically in their models. Similar forms of local intensity means and variances were also introduced in [30] for a statistical interpretation of Mumford–Shah functional. These methods were evaluated on a few images to show a certain capability of handling intensity inhomogeneity.

In this paper, we present a new region-based active contour model in a variational level set formulation for image segmentation. In our model, the local image intensities are described by Gaussian distributions with different means and variances. By using a kernel function, we first define a local energy to characterize the fitting of the local Gaussian distribution to the local image data around a neighborhood of a point. The local energy is then integrated over the entire image domain to form a double integral energy: local Gaussian distribution fitting (LGDF) energy. The local intensity means and variances, which are spatially varying functions, are two variables of the LGDF energy functional. The LGDF energy is then incorporated into a variational level set formulation with a level set regularization term. In the resulting curve evolution that minimizes the associated energy functional, the local intensity information is used to compute the means and variances and thus guide the motion of the contour toward the object boundaries. Therefore, it can be used to segment images in the presence of intensity inhomogeneity and noise. In particular, the variance as a variable

enables the proposed algorithm to distinguish regions with different intensity variances.

Note that our method is different from the methods proposed in [28–30]. First, the LGDF energy is defined as a double integral: the first integral is defined with a kernel function to characterize the fitting of the local Gaussian distribution to the local image data around a neighborhood of a point; this local energy is then integrated to form the data term as a double integral in our variational formulation. Second, the local intensity means and variances, which are two variables of the proposed energy functional, are strictly derived from a variational principle, instead of being defined empirically.

The remainder of this paper is organized as follows. Section 2 reviews several major region-based active contour models. Section 3 introduces the proposed LGDF model. In Section 4, experimental results are presented and analyzed using a set of synthetic and in vivo images. This paper is summarized in Section 5.

## 2. Background

### 2.1. Mumford–Shah functional model

Let  $\Omega \subset \mathbb{R}^2$  is the 2D image space, and  $I : \Omega \rightarrow \mathbb{R}$  be a given gray image. In [22], Mumford and Shah formulated the image segmentation problem as follows: given an image  $I$ , finding a contour  $C$  which divides the image into non-overlapping regions representing different objects. The following energy functional was proposed:

$$\mathcal{F}^{MS}(u, C) = \int_{\Omega} (u - I)^2 dx + \mu \int_{\Omega \setminus C} |\nabla u|^2 dx + \nu |C| \quad (1)$$

where  $|C|$  is the contour length,  $\mu, \nu > 0$  are constants to balance the terms.  $u$  is an image to approximate the original image  $I$ , which is smooth within each region inside or outside the contour  $C$ . The first term in Eq. (1) is the data fitting term; the second term is the smoothing term; and the third term regularizes the contour by penalizing the arc length. The minimization of Mumford–Shah functional results in an optimal contour  $C$  that segments the image  $I$  into disjointed regions, and a smoothed version of  $I$ , i.e., the denoised image  $u$ . In practice, it is difficult to solve Eq. (1) due to different dimensions of  $u$  and  $C$ . Also  $\mathcal{F}^{MS}(u, C)$  is not convex, and may have multiple local minima.

### 2.2. Chan–Vese’s PC model

To overcome the difficulties in solving Eq. (1), Chan and Vese [11] presented an active contour model based on a simplified Mumford–Shah functional. They proposed to minimize the following energy functional:

$$\mathcal{F}^{CV}(c_1, c_2, C) = \int_{outside(C)} (I - c_1)^2 dx + \int_{inside(C)} (I - c_2)^2 dx + \nu |C| \quad (2)$$

where  $outside(C)$  and  $inside(C)$  represent the regions outside and inside the contour  $C$ , respectively, and  $c_1$

and  $c_2$  are two constants that approximate the image intensity in *outside(C)* and *inside(C)*. The constants  $c_1$  and  $c_2$  can be far different from the original data, if the intensities in either *outside(C)* or *inside(C)* are not homogeneous. Consequently, the CV model generally fails to segment images with inhomogeneity. Similarly, the methods proposed in [13,15] which utilize the global image information are generally not applicable to such images either.

### 2.3. PS model

Vese and Chan [14] and Tsai et al. [12] have proposed the PS models to overcome the problems with the PC model in handling image inhomogeneities. The PS energy was defined as follows:

$$\begin{aligned} \mathcal{F}^{PS}(u^+, u^-, \phi) = & \int_{\Omega} |u^+ - I|^2 H(\phi) dx \\ & + \int_{\Omega} |u^- - I|^2 (1 - H(\phi)) dx \\ & + \mu \int_{\Omega} |\nabla u^+|^2 H(\phi) dx \\ & + \mu \int_{\Omega} |\nabla u^-|^2 (1 - H(\phi)) dx \\ & + v \int_{\Omega} |\nabla H(\phi)| dx \end{aligned} \quad (3)$$

where  $\phi$  is the level set function,  $H(\cdot)$  is Heaviside function.  $u^+$  and  $u^-$  are two smoothing functions defined on two exclusive subregions  $\Omega^+ = \{x \in \Omega : \phi(x) \geq 0\}$  and  $\Omega^- = \{x \in \Omega : \phi(x) < 0\}$ , respectively. The derived level set evolution equation is defined on the entire domain  $\Omega$ , which increases the computational burden to extend  $u^+$  and  $u^-$  to the whole image. Moreover, two extra PDEs are needed to update the functions  $u^+$  and  $u^-$  at each iteration of the level set evolution. At last, it is required to periodically re-initialize the level set function  $\phi$  to a signed distance function. Those procedures make the PS model computationally expensive [16,23].

### 2.4. The LBF model

The LBF model [25,23,31] was recently proposed to segment images with intensity inhomogeneity, using the local intensity information efficiently, and has achieved promising results. Two fitting functions  $f_1(x)$  and  $f_2(x)$  that locally approximate the intensities outside and inside the contour are introduced in the LBF model. The energy

functional is defined as follows:

$$\begin{aligned} \mathcal{F}^{LBF}(\phi, f_1, f_2) = & \lambda_1 \int \left[ \int K_{\sigma}(x-y) |I(y) - f_1(x)|^2 H(\phi(y)) dy \right] dx \\ & + \lambda_2 \int \left[ \int K_{\sigma}(x-y) |I(y) - f_2(x)|^2 (1 - H(\phi(y))) dy \right] dx \\ & + v \int |\nabla H(\phi(x))| dx + \mu \int \frac{1}{2} (|\nabla \phi(x)| - 1)^2 dx \end{aligned} \quad (4)$$

where  $\lambda_1$ ,  $\lambda_2$ ,  $v$ , and  $\mu$  are weighting positive constants.  $K_{\sigma}$  is a kernel function with a localization property that  $K_{\sigma}(u)$  decreases and approaches zero as  $|u|$  increases, and the parameter  $\sigma$  is a constant to control the local region size. The first two terms in Eq. (4) form the LBF energy. The third term is the length term to smooth the contour and the last one is the level set regularization term [7] to penalize the deviation of the level set function  $\phi$  from a signed distance function. Due to the localization property of the kernel function, the energy is dominated by the intensities  $I(y)$  in a neighborhood of  $x$ , which enables the LBF model to handle intensity inhomogeneity. However, the local intensity means do not provide enough information for accurate segmentation, especially in the presence of strong noise and intensity inhomogeneity.

As an example, Fig. 1(a) shows a synthetic image containing a circular object and background of the same intensity means but different variances. Intensity inhomogeneity was added in Fig. 1(b) and the initial contour is shown in Fig. 1(c). Fig. 1(d) shows the result of the CV model. It can be seen that the CV model fails to extract the object boundaries correctly. The means of local intensities in the background and the object are rather close to each other, according to the construction of this image. Since the LBF model only exploits local intensity means for segmentation, it fails to segment the image correctly. As we can see from the result of the LBF model shown in Fig. 1(e), a significant part of pixels in the object are mislabeled as the background. In order to accurately extract the object boundary, more complete statistical characteristics of local intensities has to be taken into account. This is the main goal of this paper.

## 3. Local Gaussian distribution fitting

In this section, we propose an implicit active contour model based on local intensity distribution. To effectively exploit information on local intensities, we need to

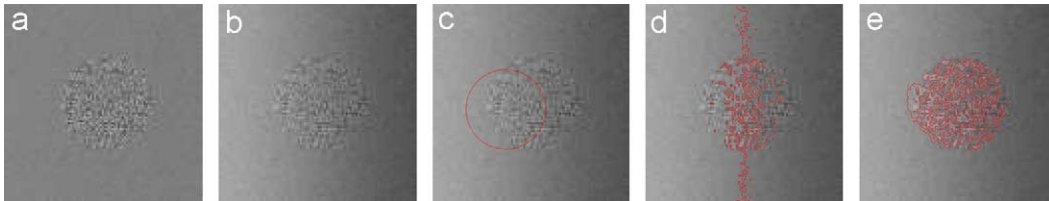


**Fig. 1.** Experiments for a synthetic image: (a) original image with the same intensity means but different variances for the object and background; (b) synthetic image obtained by adding intensity inhomogeneity to (a); (c) initial contour; (d) result of the CV model; (e) result of the LBF model.

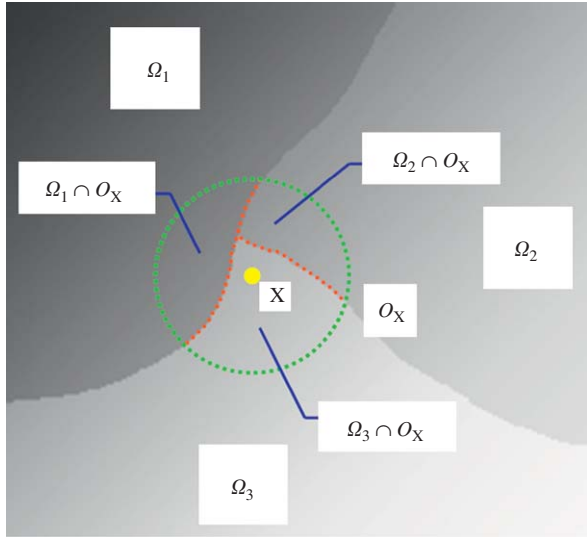


**Fig. 2.** Graphical representation of  $\Omega_i \cap \mathcal{O}_x$ . The dashed green circle denotes the circular neighborhood of  $x$ ,  $\mathcal{O}_x$ .  $\Omega_1$ ,  $\Omega_2$ , and  $\Omega_3$  partition  $\mathcal{O}_x$  into three subregions  $\Omega_1 \cap \mathcal{O}_x$ ,  $\Omega_2 \cap \mathcal{O}_x$ , and  $\Omega_3 \cap \mathcal{O}_x$ . (For interpretation of the references to color in this figure legend, the reader is referred to the web version of this article.)

characterize the distribution of local intensities via partition of neighborhood as in [17]. For each point  $x$  in the image domain  $\Omega$ , we consider a circular neighborhood with a small radius  $\rho$ , which is defined as  $\mathcal{O}_x \triangleq \{y : |x - y| \leq \rho\}$ . Let  $\{\Omega_i\}_{i=1}^N$  denote a set of disjoint image regions, such that  $\Omega = \bigcup_{i=1}^N \Omega_i$ ,  $\Omega_i \cap \Omega_j = \emptyset$ ,  $\forall i \neq j$ , where  $N$  refers to the number of regions. The regions  $\{\Omega_i\}_{i=1}^N$  produce a partition of the neighborhood  $\mathcal{O}_x$ , i.e.,  $\{\Omega_i \cap \mathcal{O}_x\}_{i=1}^N$ . For example, Fig. 2 presents an image consisting of three regions:  $\Omega_1$ ,  $\Omega_2$  and  $\Omega_3$ , which divide the region  $\mathcal{O}_x$  into three subregions as  $\Omega_1 \cap \mathcal{O}_x$ ,  $\Omega_2 \cap \mathcal{O}_x$ , and  $\Omega_3 \cap \mathcal{O}_x$ . Now, we consider the segmentation of this circular neighborhood  $\mathcal{O}_x$  based on *maximum a posteriori probability* (MAP). Let  $p(y \in \Omega_i \cap \mathcal{O}_x | I(y))$  be the *a posteriori* probability of the subregions  $\Omega_i \cap \mathcal{O}_x$  given the neighborhood gray values  $I(y)$ .

According to the Bayes rule:

$$p(y \in \Omega_i \cap \mathcal{O}_x | I(y)) = \frac{p(I(y) | y \in \Omega_i \cap \mathcal{O}_x) p(y \in \Omega_i \cap \mathcal{O}_x)}{p(I(y))} \quad (5)$$

where  $p(I(y) | y \in \Omega_i \cap \mathcal{O}_x)$ , denoted by  $p_{i,x}(I(y))$ , is the probability density in region  $\Omega_i \cap \mathcal{O}_x$ , i.e., the gray value distribution within this region.  $p(y \in \Omega_i \cap \mathcal{O}_x)$  is the *a priori* probability of the partition  $\Omega_i \cap \mathcal{O}_x$  among all possible partitions of  $\mathcal{O}_x$ , and  $p(I(y))$  is the *a priori* probability of gray value  $I(y)$ , which is independent of the choice of the region and can therefore be neglected.

Given all partitions are *a priori* equally possible [13], i.e.,  $p(y \in \Omega_i \cap \mathcal{O}_x) = 1/N$ , the term  $p(y \in \Omega_i \cap \mathcal{O}_x)$  can be ignored. Assuming that the pixels within each region are independent [13], the MAP will be achieved only if the product of  $p_{i,x}(I(y))$  across the regions  $\mathcal{O}_x$  is maximized:

$$\prod_{i=1}^N \prod_{y \in \Omega_i \cap \mathcal{O}_x} p_{i,x}(I(y)) \quad (6)$$

Taking a logarithm, the maximization can be converted to the minimization of the following energy, denoted by  $E_x^{LGDF}$ :

$$E_x^{LGDF} = \sum_{i=1}^N \int_{\Omega_i \cap \mathcal{O}_x} -\log p_{i,x}(I(y)) dy \quad (7)$$

There are various approaches to model the probability densities  $p_{i,x}(I(y))$ , including Gaussian density with fixed standard deviation [11], a full Gaussian density [32,15], or non-parametric Parzen estimator [33,34]. Most image segmentation methods assume a global model for the probability of each region, i.e., the probability density function only depends on the region but does not change within one region [29]. Consequently, these methods have difficulties in the presence of intensity inhomogeneity. In this paper, we assume the mean and variance of the local Gaussian distribution are spatially varying parameters, i.e.,

$$p_{i,x}(I(y)) = \frac{1}{\sqrt{2\pi}\sigma_i(x)} \exp\left(-\frac{(u_i(x) - I(y))^2}{2\sigma_i(x)^2}\right) \quad (8)$$

where  $u_i(x)$  and  $\sigma_i(x)$  are local intensity means and standard deviations, respectively.

By introducing a weighting function into the function (7), we define the following objective functional:

$$E_x^{LGDF} = \sum_{i=1}^N \int_{\Omega_i \cap \mathcal{O}_x} -\omega(x - y) \log p_{i,x}(I(y)) dy \quad (9)$$

where  $\omega(x - y)$  is a non-negative weighting function such that  $\omega(x - y) = 0$  for  $|x - y| > \rho$  and  $\int_{\mathcal{O}_x} \omega(x - y) dy = 1$ . Although the choice of the weighting function is flexible, it is preferable to use a weighting function  $\omega(x - y)$  such that larger weights are assigned to the data  $I(y)$  for  $y$  closer to the center  $x$  of the neighborhood  $\mathcal{O}_x$ . In this paper, the weighting function  $\omega$  is chosen as a truncated Gaussian kernel with a localization property that  $\omega(d)$  decreases and approaches zero as  $|d|$  increases,

$$\omega(d) = \begin{cases} \frac{1}{a} \exp\left(-\frac{|d|^2}{2\sigma^2}\right) & \text{if } |d| \leq \rho \\ 0 & \text{if } |d| > \rho \end{cases}$$

where  $a$  is a constant such that  $\int \omega(d) = 1$ . The above objective function  $E_x^{LGDF}$  can be rewritten as

$$E_x^{LGDF} = \sum_{i=1}^N \int_{\Omega_i} -\omega(x - y) \log p_{i,x}(I(y)) dy \quad (10)$$

due to the localization property of the weighting function, namely,  $\omega(x - y) = 0$  for  $y \notin \mathcal{O}_x$ . Note that similar localized objective function using a kernel was introduced in [25,23] for a level set-based image segmentation method.

The ultimate goal is to minimize  $E_x^{LGDF}$  for all the center points  $x$  in the image domain  $\Omega$ , which directs us to define the following double integral energy functional:

$$E^{LGDF} = \int_{\Omega} E_x^{LGDF} dx = \int_{\Omega} \left( \sum_{i=1}^N \int_{\Omega_i} -\omega(x - y) \log p_{i,x}(I(y)) dy \right) dx \quad (11)$$

**Remark.** The proposed method is essentially different from the methods in [28–30] for the following reasons. First, we introduced a localized energy functional using a truncated Gaussian kernel. Second, the energy in our method is a double integral, whereas the energy in [28–30] is a single integral. They simply used spatially varying means and variances to replace the constant means and variances in a globally defined energy as in [32,15,13], without using a Gaussian kernel or any localized energy. However, in their implementation, the Gaussian kernel is introduced to compute spatially varying means and variances, which is not consistent with the theory.

### 3.1. Level set formulation

We assume that the image domain can be partitioned into two regions: foreground and background, denoted by  $\Omega_1$  and  $\Omega_2$ , respectively. These two regions can be represented as the regions outside and inside the zero level set of  $\phi$ , i.e.,  $\Omega_1 = \{\phi > 0\}$  and  $\Omega_2 = \{\phi < 0\}$ . Using Heaviside function  $H$ , the energy  $E_x^{LGDF}$  in Eq. (10) can be expressed as an energy in terms of  $\phi$ ,  $u_i$ , and  $\sigma_i^2$

$$\begin{aligned} E_x^{LGDF}(\phi, u_1(x), u_2(x), \sigma_1(x)^2, \sigma_2(x)^2) \\ = - \int \omega(x-y) \log p_{1,x}(I(y)) M_1(\phi(y)) dy \\ - \int \omega(x-y) \log p_{2,x}(I(y)) M_2(\phi(y)) dy \end{aligned} \quad (12)$$

where  $M_1(\phi(y)) = H(\phi(y))$  and  $M_2(\phi(y)) = 1 - H(\phi(y))$ . Thus, the energy  $E^{LGDF}$  in Eq. (11) can be rewritten as

$$\begin{aligned} E^{LGDF}(\phi, u_1, u_2, \sigma_1^2, \sigma_2^2) \\ = \int_{\Omega} E_x^{LGDF}(\phi, u_1(x), u_2(x), \sigma_1(x)^2, \sigma_2(x)^2) dx \end{aligned} \quad (13)$$

For more accurate computation involving the level set function and its evolution, we need to regularize the level set function by penalizing its deviation from a signed distance function [7], characterized by the following energy functional:

$$\mathcal{P}(\phi) = \int \frac{1}{2} (|\nabla \phi(x)| - 1)^2 dx \quad (14)$$

As in typical level set methods, we need to regularize the zero level set by penalizing its length to derive a smooth contour during evolution:

$$\mathcal{L}(\phi) = \int |\nabla H(\phi(x))| dx \quad (15)$$

Therefore, the entire energy functional is

$$\begin{aligned} \mathcal{F}(\phi, u_1, u_2, \sigma_1^2, \sigma_2^2) = E^{LGDF}(\phi, u_1, u_2, \sigma_1^2, \sigma_2^2) \\ + v \mathcal{L}(\phi) + \mu \mathcal{P}(\phi) \end{aligned} \quad (16)$$

where  $v, \mu > 0$  are weighting constants.

In practice, Heaviside function  $H$  is approximated by a smoothing function  $H_\varepsilon$  defined by

$$H_\varepsilon(x) = \frac{1}{2} \left[ 1 + \frac{2}{\pi} \arctan\left(\frac{x}{\varepsilon}\right) \right] \quad (17)$$

and the derivative of  $H_\varepsilon$  is the following smoothing function:

$$\delta_\varepsilon(x) = H'_\varepsilon(x) = \frac{1}{\pi} \frac{\varepsilon}{\varepsilon^2 + x^2} \quad (18)$$

Thus, the energy functional  $\mathcal{F}(\phi, u_1, u_2, \sigma_1^2, \sigma_2^2)$  in Eq. (16) is approximated by

$$\begin{aligned} \mathcal{F}_\varepsilon(\phi, u_1, u_2, \sigma_1^2, \sigma_2^2) = E_\varepsilon^{LGDF}(\phi, u_1, u_2, \sigma_1^2, \sigma_2^2) \\ + v \mathcal{L}_\varepsilon(\phi) + \mu \mathcal{P}(\phi) \end{aligned} \quad (19)$$

**Remark.** The CV model and the LBF model can be considered as special cases of our model. In fact, if  $\sigma_1$  and  $\sigma_2$  in Eq. (8) are both equal to  $\sqrt{0.5}$ , it will be the same as the LBF model. Moreover, if  $\sigma_1 = \sigma_2 = \sqrt{0.5}$ , and  $\sigma \rightarrow \infty$ , it will be the same as the CV model.

### 3.2. Gradient descent flow

By calculus of variations, it can be shown that the parameters  $u_i$  and  $\sigma_i^2$  that minimize the energy functional in Eq. (19) satisfy the following Euler–Lagrange equations:

$$\int \omega(y-x)(u_i(x) - I(y)) M_{i,\varepsilon}(\phi(y)) dy = 0 \quad (20)$$

and

$$\int \omega(y-x)(\sigma_i(x)^2 - (u_i(x) - I(y))^2) M_{i,\varepsilon}(\phi(y)) dy = 0 \quad (21)$$

where  $M_{1,\varepsilon}(\phi(y)) = H_\varepsilon(\phi(y))$  and  $M_{2,\varepsilon}(\phi(y)) = 1 - H_\varepsilon(\phi(y))$ .

From (20) and (21), we obtain

$$u_i(x) = \frac{\int \omega(y-x) I(y) M_{i,\varepsilon}(\phi(y)) dy}{\int \omega(y-x) M_{i,\varepsilon}(\phi(y)) dy} \quad (22)$$

and

$$\sigma_i(x)^2 = \frac{\int \omega(y-x)(u_i(x) - I(y))^2 M_{i,\varepsilon}(\phi(y)) dy}{\int \omega(y-x) M_{i,\varepsilon}(\phi(y)) dy} \quad (23)$$

which minimize the energy functional  $\mathcal{F}_\varepsilon(\phi, u_1, u_2, \sigma_1^2, \sigma_2^2)$  for a fixed  $\phi$ .

Note that the formulas of  $u_i(x)$  and  $\sigma_i(x)^2$  in Eqs. (22) and (23) are also presented in [28–30], which are, however, empirically defined, instead of being derived from a variational principle.

Minimization of the energy functional  $\mathcal{F}_\varepsilon$  in Eq. (19) with respect to  $\phi$  can be achieved by solving the gradient descent flow equation (see Appendix for detailed derivation)

$$\begin{aligned} \frac{\partial \phi}{\partial t} = - \delta_\varepsilon(\phi)(e_1 - e_2) + v \delta_\varepsilon(\phi) \operatorname{div} \left( \frac{\nabla \phi}{|\nabla \phi|} \right) \\ + \mu \left( \nabla^2 \phi - \operatorname{div} \left( \frac{\nabla \phi}{|\nabla \phi|} \right) \right) \end{aligned} \quad (24)$$

where

$$e_1(x) = \int_{\Omega} \omega(y-x) \left[ \log(\sigma_1(y)) + \frac{(u_1(y) - I(x))^2}{2\sigma_1(y)^2} \right] dy \quad (25)$$

and

$$e_2(x) = \int_{\Omega} \omega(y-x) \left[ \log(\sigma_2(y)) + \frac{(u_2(y) - I(x))^2}{2\sigma_2(y)^2} \right] dy \quad (26)$$



Note that the image-based term  $(e_1 - e_2)$  is independent of scale of local intensities caused by intensity inhomogeneity. According to the analysis of local intensities in [17], the observed intensities  $\bar{I}(y)$  in  $\mathcal{O}_x$  can be approximated by  $bI(y)$ , where  $b$  is the scaling factor. Therefore, the new local intensity means  $u_i(x)$  and standard deviations  $\sigma_i(x)$  are multiplied by  $b$ :  $u_i(x) = bu_i(y)$ ,  $\sigma_i(x) = b\sigma_i(y)$ , transforming the new image-based terms as  $(\bar{e}_1 - \bar{e}_2)$ :

$$\begin{aligned}
 & (\bar{e}_1 - \bar{e}_2) \\
 &= \int_{\Omega} \omega(y-x) \left[ \log(b\sigma_1(y)) + \frac{(bu_1(y) - bI(x))^2}{2(b\sigma_1(y))^2} \right] dy \\
 &\quad - \int_{\Omega} \omega(y-x) \left[ \log(b\sigma_2(y)) + \frac{(bu_2(y) - bI(x))^2}{2(b\sigma_2(y))^2} \right] dy \\
 &= \int_{\Omega} \omega(y-x) \left[ \log(\sigma_1(y)) + \frac{(u_1(y) - I(x))^2}{2\sigma_1(y)^2} \right] dy \\
 &\quad - \int_{\Omega} \omega(y-x) \left[ \log(\sigma_2(y)) + \frac{(u_2(y) - I(x))^2}{2\sigma_2(y)^2} \right] dy \\
 &= (e_1 - e_2)
 \end{aligned} \tag{27}$$

This property shows that the influence of the image-based term  $(e_1 - e_2)$  is invariant to contrast change caused by intensity inhomogeneity. Note that a similar property was also given in [28] for a related model.

#### 4. Implementation and experiment results

The implementation of our method is straightforward. The proposed iterative procedure is presented below:

- Step 1: Initialize a level set function  $\phi$ .
- Step 2: Update local means  $u_i(x)$  using Eq. (22).
- Step 3: Update local variances  $\sigma_i(x)^2$  using Eq. (23).
- Step 4: Update the level set function  $\phi$  according to Eq. (24).
- Step 5: Return to step 2 until the convergence criteria is met.

To compute the convolutions in Eqs. (22) and (23) more efficiently, the kernel  $\omega$  is truncated as a  $(2\rho + 1) \times (2\rho + 1)$  mask, where  $\rho$  is no less than  $2\sigma$ . The image-based term  $(e_1 - e_2)$  in Eq. (24) can be written as a linear combination of three convolutions. All the partial derivatives  $\partial\phi/\partial x$  and  $\partial\phi/\partial y$  in Eq. (24) can be simply discretized as central finite differences. The temporal derivative is discretized as a forward difference. An iteration scheme is then followed by discretizing the PDE (24). The level set function  $\phi$  can be simply initialized as a binary step function as in [7], which takes a negative constant value  $-c_0$  inside the region  $R_0$  and a positive constant value  $c_0$  outside it. We choose  $c_0 = 2$  in the experiments. The proposed method has been tested with synthetic and real images of different modalities. Unless otherwise specified, we use the following default setting of the parameters in the experiments:  $\sigma = 3.0$ ,  $\rho = 6$ , time step  $\Delta t = 0.1$ ,  $\mu = 1.0$ , and  $\nu = 0.0001 \times 255 \times 255$  for all images in this work.

Experimental result performed on synthetic image is presented in Fig. 3. Note that this image is the same image in Fig. 1(b), which has shown that the CV model and the LBF model failed to extract the object boundary. Using the

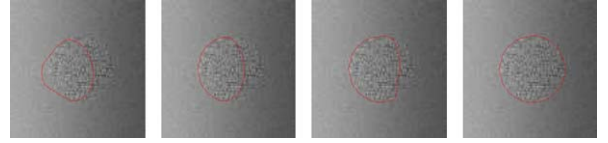


Fig. 3. Intermediate results of our method for Fig. 1(b).

same initialization in Fig. 1(c), the intermediate results of our LGDF algorithm are presented in Fig. 3. Although the local mean intensities are similar, the local intensity variances are distinct, which enables our model to distinguish the background and foreground, as shown in the last image of Fig. 3.

Fig. 4(a) shows a fish-shaped image, and Fig. 4(b) is obtained by corrupting Fig. 4(a) with severe intensity inhomogeneity. It can be seen from Fig. 4(a), the intensity in the background decreases gradually from the left to the right. Using the initial contour in Fig. 4(c), the intermediate results of the PS model [14], LBF model, and our method are shown in the second, third and fourth row, respectively. The result of the CV model is also shown in Fig. 4(d). It can be observed that the CV model which assumes that an image consists of homogeneous regions fails to extract the object boundary. Compared to the CV model, the PS model and the LBF model achieve better results. However, the PS model and the LBF model fail to extract the whole object boundaries due to the low image contrast in the right side of the image. By contrast, our method is less dependent from image contrast. The result of our method is satisfactory as shown in the last row of Fig. 4.

##### 4.1. Application on real images

Fig. 5 presents the results for real-world images. The images in the first two rows are corrupted by intensity inhomogeneity due to non-uniform illumination, which is often seen in camera images. The third row shows the result of rice image corrupted by intensity inhomogeneity. It can be seen that the new contours can emerge during the evolution to extract multiple object boundaries. The fourth and fifth rows in Fig. 5 show the results of our method on two infrared images, which include some rather weak boundaries. Moreover, significant intensity variations exist in these infrared images, which renders a difficult task to recover the whole object boundary if it relies on local intensity means alone. Nevertheless, our method successfully extracts the object boundaries for these images.

##### 4.2. Application on medical images

We also evaluated the performance of the algorithm on a set of in vivo medical images. The first two rows of Fig. 6 show two vessel images with intensity inhomogeneity. In these vessel images, some vessel boundaries are quite weak. The third row shows the left ventricle in a tagged MR image. It is clearly seen that the image is corrupted by noise, severe intensity inhomogeneity

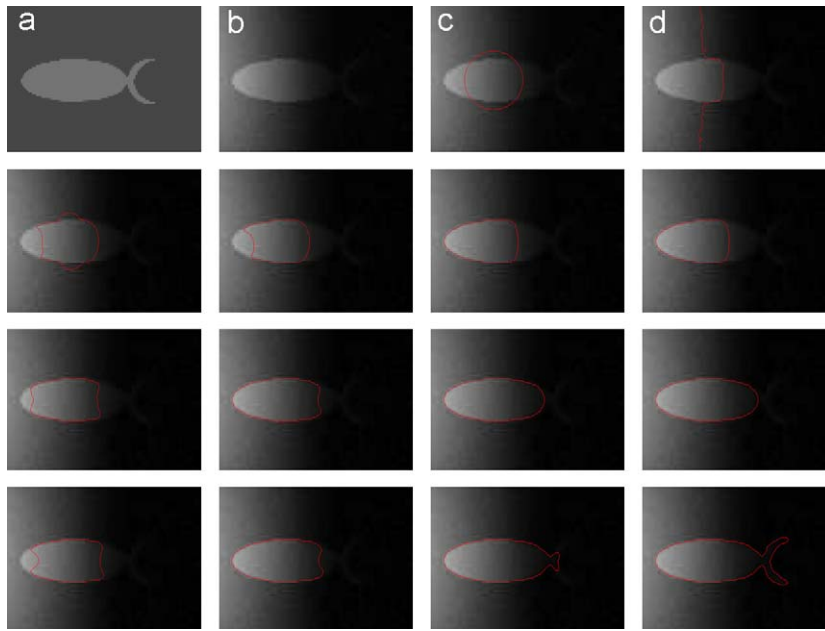


**Fig. 4.** Comparison of our method with the CV, PS, and LBF model: (a) synthetic image; (b) is obtained by corrupting (a) with severe intensity inhomogeneity; (c) initial contour; (d) result of the CV model. Rows 2, 3, and 4 show the intermediate results of the PS model, LBF model and our method.

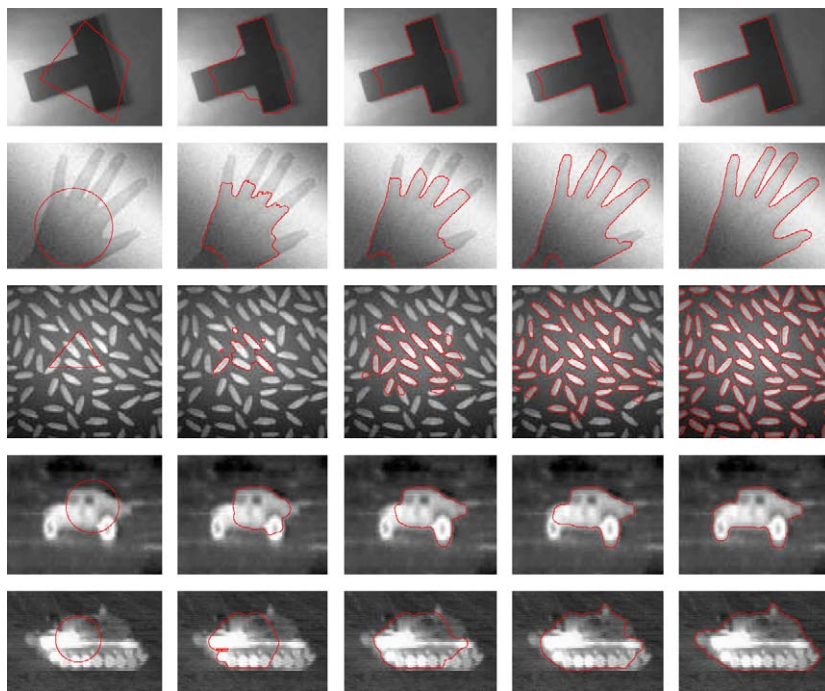


**Fig. 5.** Results of our method for real images. The curve evolution process from the initial contour (in the first column) to the final contour (in the fifth column) is shown in every row for the corresponding image.

and weak boundaries. For this image, we set  $\nu = 0.0008 \times 255 \times 255$ . The fourth row shows the tumor segmentation result of a brain image. In this case tumor boundaries are quite weak. Our method has also been applied to ultrasound images, which usually include speckle noise and low signal-to-noise

ratio. The last two rows show the results of our method for ultrasound images of carotid artery and left ventricle. The boundaries of the carotid artery and ventricle are successfully delineated by our method despite the presence of strong noise. For last two ultrasound images, we set  $\nu = 0.0005 \times 255 \times 255$ . In all

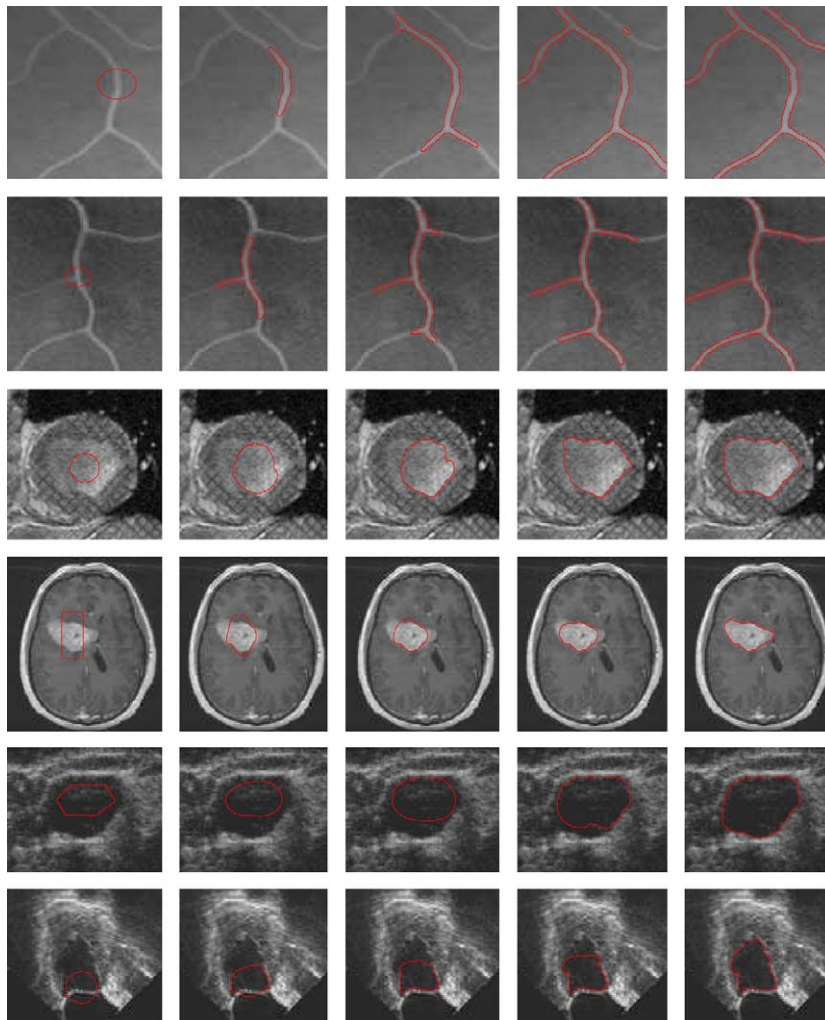


**Fig. 6.** Results of our method for medical images. The curve evolution process from the initial contour (in the first column) to the final contour (in the fifth column) is shown in every row for the corresponding image.

these images, our model accurately recovers the object shapes.

#### 4.3. Comparisons with the CV model, the LBF model and mean shift algorithm

A comparison of the accuracy in delineating the true boundary of the objects is performed between our approach and two major approaches: the CV model and the LBF model. The PS model is not compared here due to its expensive computational cost [16,23]. Fig. 7 shows the results of the CV model (the upper row), the LBF model (the lower row). Note that the initial contours are the same as the first column of Fig. 6. Based on only global intensity information, the CV model fails to segment those images. Using a local intensity model, the LBF model performs better on these images (especially for the first vessel image). However, with only local intensity means, the LBF model fails to segment the left ventricle image

and last two ultrasound images which have severe intensity inhomogeneity and noise problems. By contrast, our method successfully extracts object boundaries for these images, as shown in last column of Fig. 6.

We now focus on comparing our model with the well-known mean shift algorithm [35], which to certain extent can handle intensity inhomogeneity. To compare with the mean shift algorithm, we used the software EDISON download from <http://www.caip.rutgers.edu/riul/research/code/EDISON>, which is based on a fast implementation of the mean shift algorithm using a speed-up scheme described in [36]. Fig. 8 shows the results of mean shift algorithm for the same images in Fig. 7. The results of mean shift algorithm for the first two images are similar to that of our method. However, for these vessel images, small portions of the vessel are missing. For the rest four images, the errors of mean shift algorithm are obvious. We notice that the mean shift algorithm is somewhat sensitive to the choice of two major parameters: spatial bandwidth  $h_s$  and range bandwidth  $h_r$ . We have carefully



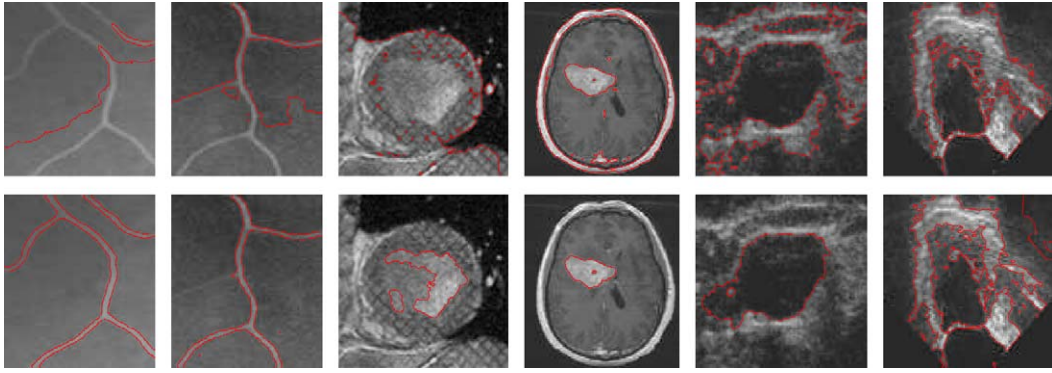


**Fig. 7.** Comparisons of our method with the CV model and the LBF model. Upper row: results of the CV model; lower row: results of the LBF model.

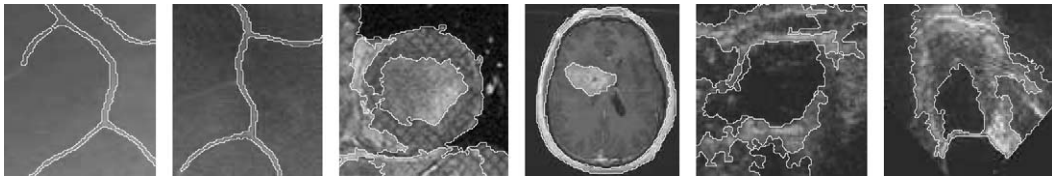


**Fig. 8.** Results of mean shift algorithm for the images in Fig. 6 with spatial bandwidth  $h_s$  and the range bandwidth  $h_r$  represented as a pair  $(h_s; h_r) = (4; 2); (4; 4); (7; 4); (5; 4); (5; 5);$  and  $(6; 6)$  from left to right.

tweaked these two parameters to obtain the best segmentation results as we can.

#### 4.4. Robustness to intensity inhomogeneity

In order to further demonstrate the capability of our method in dealing with intensity inhomogeneity, we test our method for two brain MR images of the same object with increased intensity inhomogeneity (Fig. 9). The image in the upper row exhibits obvious intensity inhomogeneity. The LBF model successfully extracts white matter boundaries for this image. The image in the lower row exhibits more severe intensity inhomogeneity. For this image, the local intensity means of  $f_1(x)$  and  $f_2(x)$  are rather close which results in an unclear decision on the boundaries of white matter. Consequently, the LBF model fails to extract white matter from the image. Fig. 10 shows the intermediate results of our method with the same initial contours as in Fig. 9. It can be seen that our method achieves satisfactory results for these images. It can be observed that the new contours emerge easily, which speeds up the evolution toward final results. This experiment shows the robustness of our method to intensity inhomogeneity.

#### 4.5. Results for synthetic noisy images

To test the performance of our method in the presence of noise, we apply it to synthetic images with different strengths of noise. We first test on the images with additive noise. The top row of Fig. 11 shows a synthetic image, where the exact location of the object boundary is known (indicated by the red curve). The second row

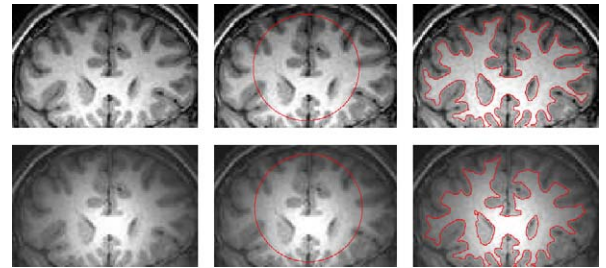


**Fig. 9.** Two brain MR images with increased intensity inhomogeneity. Column 1: original images. Column 2: initial contours. Column 3: results of the LBF model.

shows four noisy images obtained by adding Gaussian noise with standard deviations 10, 15, 20, 25 to the synthetic image. The results of the proposed method are shown in the third row. For comparison, the results of the method by Rosenhahn et al. [29] are shown in the fourth row. Note that the second row of Fig. 11 shows the initial contours used for both our model and the method by Rosenhahn et al. It can be observed that the results of our model and Rosenhahn et al.'s model look similar. However, we can show by quantitative comparison that our model produces more accurate results than the Rosenhahn et al.'s model. The metric adopted in this paper for comparison is the root mean squared error (RMSE), which measures a distance between the reconstructed contours (i.e., the final contours of both models) and the exact object boundary. Let the coordinates of the points on the reconstructed contour are  $(x_0, y_0), \dots, (x_{n-1}, y_{n-1})$ . For the point  $(x_k, y_k)$  ( $k = 0, \dots, n-1$ ), we found the corresponding point  $(\bar{x}_k, \bar{y}_k)$  ( $k = 0, \dots, n-1$ ) on the ground truth curve that has the closest distance from

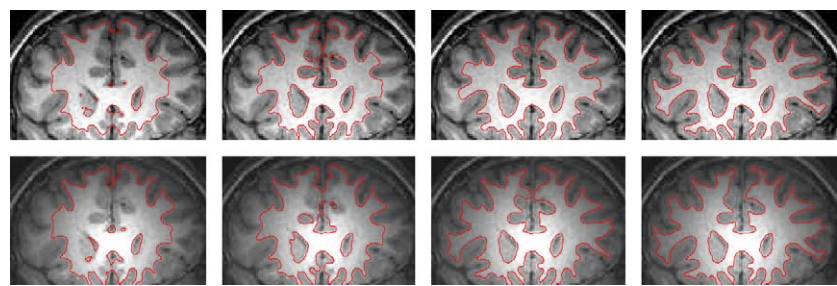


**Fig. 10.** Results of our method for brain MR images shown in Fig. 9. The curve evolution process from the initial contour (the first column) to the final contour (the fourth column) is shown in every row.

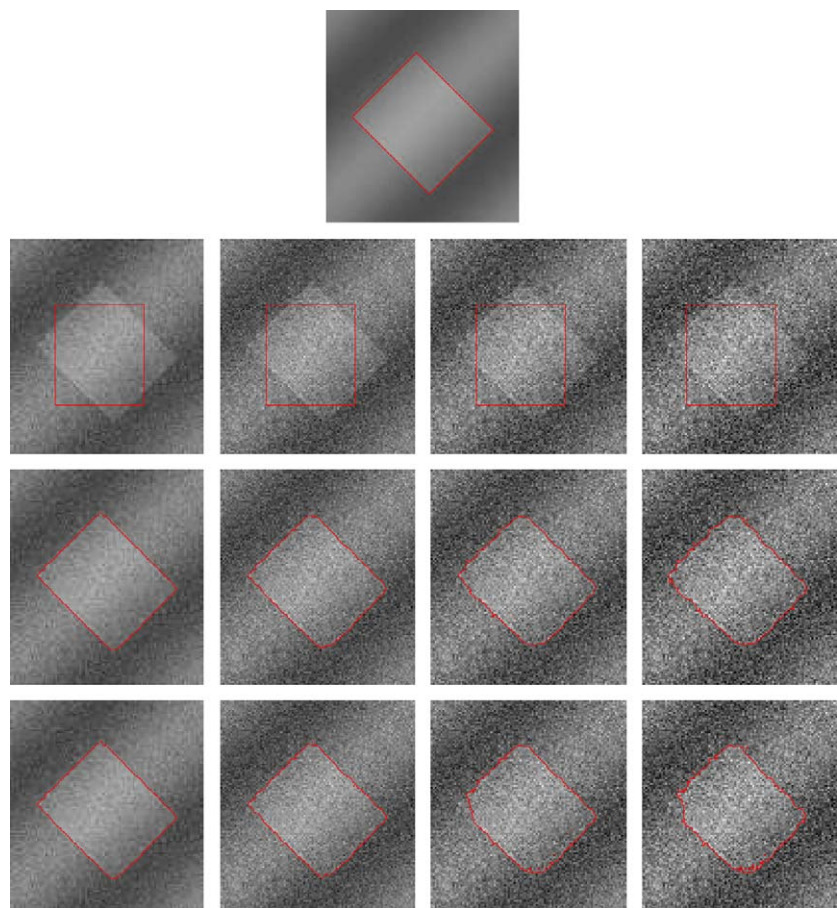


**Fig. 11.** Results for the images corrupted by additive Gaussian noise. Row 1: synthetic image. Row 2: noisy images with standard deviations 10, 15, 20, 25 and the initial contours. Row 3: results of the proposed method. Row 4: results of the method by Rosenhahn et al. [29].

point  $(x_k, y_k)$  ( $k = 0, \dots, n - 1$ ). Then the RMSE is computed as follows:

$$RMSE = \sqrt{\frac{\sum_{k=0}^{n-1} [(x_k - \bar{x}_k)^2 + (y_k - \bar{y}_k)^2]}{n}}$$

The RMSE values are listed in Table 1. This quantitative comparison shows the superiority of our model over Rosenhahn et al.'s approach in terms of segmentation accuracy.

Our method also work well for images with multiplicative noise. The top row of Fig. 12 shows the images

**Table 1**  
RMSE values for the images in the second row of Fig. 11 in the same order.

	Image 1	Image 2	Image 3	Image 4
Proposed method	0.23	0.48	0.70	0.98
Method by Rosenhahn et al.	0.34	0.53	1.27	1.64

contaminated with multiplicative Gaussian noise with standard deviations of (0.1, 0.15, 0.2 and 0.25). The results of the proposed method and the method by

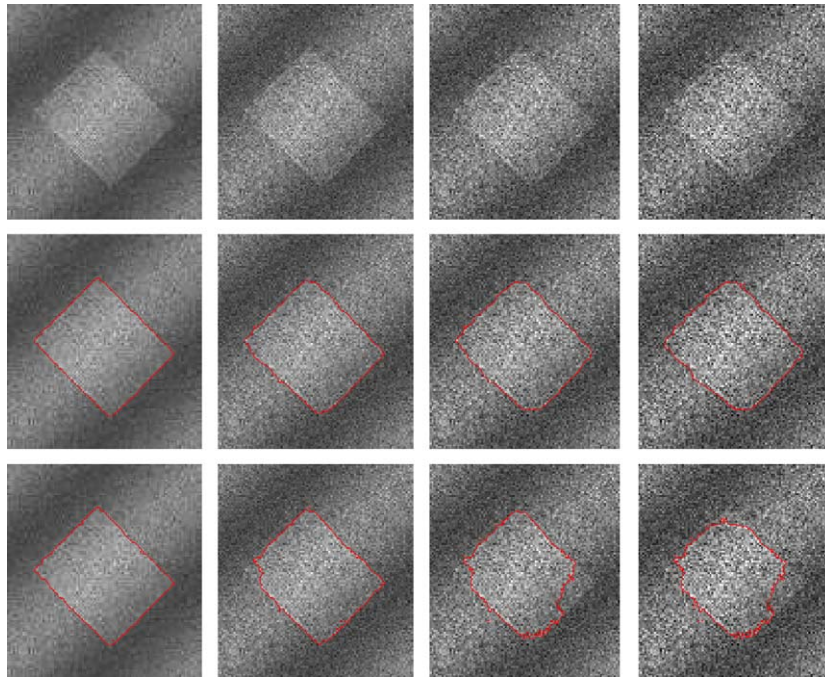


**Fig. 12.** Results for the images corrupted by multiplicative Gaussian noise. Row 1: noisy images with standard deviations 0.1, 0.15, 0.2, and 0.25. Row 2: results of the proposed method. Row 3: results of the method by Rosenhahn et al. [29].

**Table 2**

RMSE values for the images in Fig. 12 in the same order.

	Image 1	Image 2	Image 3	Image 4
Proposed method	0.06	0.48	0.65	1.42
Method by Rosenhahn et al.	0.21	1.91	11.7	12.54

Rosenhahn et al. are presented in the second and third rows, respectively. The RMSE values for these images are listed in Table 2. It can be observed that our model yields more accurate results than Rosenhahn et al.'s approach.

#### 4.6. Application on natural texture images

With the comprehensive local statistic model, our model can capture the texture features, therefore can be applied to some texture images. Fig. 13 shows some results for natural texture images. It can be observed that the variances of objects and background are distinct, which enables our method to extract the objects. The first row shows an image with a tiger in the water. The intensities of the background are not uniform due to illumination change. The second row shows the result of a leopard segmentation. It can be seen that the pattern of leopard is similar to that of the background, which renders a non-trivial task to recover the complete object boundary. The last row shows the segmentation result of two zebras. The dark shadow in the background could be incorrectly segmented as the object. In fact, the local

variances of zebras and the black shadow are distinct. Therefore, our method can successfully extract the objects from the background.

#### 4.7. Computational time

The proposed method requires relatively high computational complexity  $O(S_1 S_2)$ , where  $S_1$  and  $S_2$  are the size of the image and kernel, respectively. Table 3 presents the details about the computational time and number of iterations to process the images presented in Fig. 5. The images were analyzed in a 2.8 GHz PC (Pentium 4) loaded with Matlab 7.1.

### 5. Conclusion

In this paper, we have proposed a novel region-based active contour model for image segmentation in a variational level set framework. Our model efficiently utilizes the local image intensities which are described by Gaussian distribution with different means and variances. The local intensity means and variances are spatially varying functions, which are introduced as two variables of the proposed energy functional in our model. As a result, our method is able to deal with both noise and intensity inhomogeneity. Comparisons with the PC model, LBF model, and mean shift algorithm clearly demonstrate the capability of our method in handling intensity inhomogeneity. In addition, this method can be applied to some texture images.



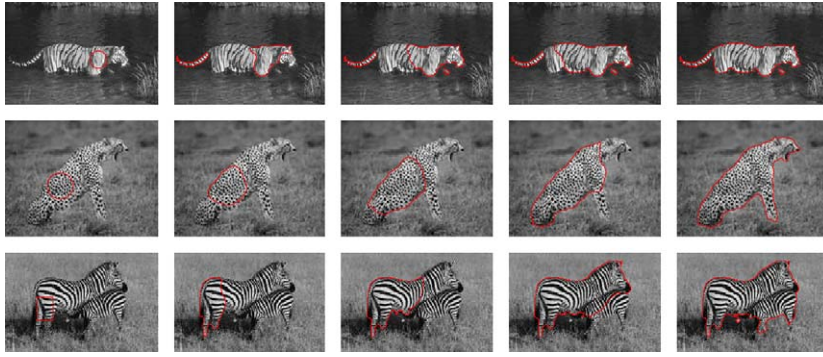


**Fig. 13.** Results of our method for texture images. The curve evolution process from the initial contour (in the first column) to the final contour (in the fifth column) is shown in every row for the corresponding image.

**Table 3**

CPU time (in s) for our model for the images in Fig. 5 in the same order.

Image	Image 1	Image 2	Image 3	Image 4	Image 5
Size	113 × 150	99 × 120	128 × 128	93 × 118	103 × 157
Iteration	365	550	110	270	310
CPU time	25.22	27.37	7.55	13.79	21.09

## Appendix A. Derivation of gradient flow

A standard method to minimize an energy functional  $F(\phi)$  is to solve the gradient flow equation

$$\frac{\partial \phi}{\partial t} = -\frac{\partial F}{\partial \phi} \quad (28)$$

where  $\partial F / \partial \phi$  is the Gâteaux derivative (cf. [37]) of the energy functional  $F(\phi)$ . Note that the second term and the third term in (19) and their Gâteaux derivatives have been given in [11,7], we only need to derive the Gâteaux derivative of the first term. By exchanging the order of integration,  $E_e^{LGDF}$  can be rewritten as

$$\begin{aligned}
 E_e^{LGDF} &= - \int \left[ \int \omega(x-y) \log \left( \frac{1}{\sqrt{2\pi}\sigma_1(x)} \exp \left( -\frac{(u_1(x)-I(y))^2}{2\sigma_1(x)^2} \right) \right) \right. \\
 &\quad \times H_e(\phi(y)) dx \Big] dy \\
 &\quad - \int \left[ \int \omega(x-y) \log \left( \frac{1}{\sqrt{2\pi}\sigma_2(x)} \exp \left( -\frac{(u_2(x)-I(y))^2}{2\sigma_2(x)^2} \right) \right) \right. \\
 &\quad \times (1 - H_e(\phi(y))) dx \Big] dy \\
 &= \int \left[ \int \omega(x-y) \left( \log(\sqrt{2\pi}) + \log(\sigma_1(x)) + \frac{(u_1(x)-I(y))^2}{2\sigma_1(x)^2} \right) dx \right] \\
 &\quad \times H_e(\phi(y)) dy \\
 &\quad + \int \left[ \int \omega(x-y) \left( \log(\sqrt{2\pi}) + \log(\sigma_2(x)) + \frac{(u_2(x)-I(y))^2}{2\sigma_2(x)^2} \right) dx \right] \\
 &\quad \times (1 - H_e(\phi(y))) dy \quad (29)
 \end{aligned}$$

Let  $e_1(y) = \int \omega(x-y)(\log(\sigma_1(x)) + (u_1(x)-I(y))^2/2\sigma_1(x)^2) dx$  and  $e_2(y) = \int \omega(x-y)(\log(\sigma_2(x)) + (u_2(x)-I(y))^2/2\sigma_2(x)^2) dx$ . By calculus of variations [37], it is straightforward to derive the Gâteaux derivative of the energy  $E_e^{LGDF}$

in (29) as below

$$\frac{\partial E_e^{LGDF}}{\partial \phi} = e_1 \delta_e(\phi) - e_2 \delta_e(\phi) \quad (30)$$

A combination of the Gâteaux derivatives of the three terms in entire energy functional (19) yields

$$\begin{aligned}
 \frac{\partial \mathcal{F}_e}{\partial \phi} &= \delta_e(\phi)(e_1 - e_2) - v \delta_e(\phi) \operatorname{div} \left( \frac{\nabla \phi}{|\nabla \phi|} \right) \\
 &\quad - \mu \left( \nabla^2 \phi - \operatorname{div} \left( \frac{\nabla \phi}{|\nabla \phi|} \right) \right) \quad (31)
 \end{aligned}$$

Using (28) for the energy functional  $\mathcal{F}_e$ , we obtain its gradient flow (24).

## References

- [1] M. Kass, A. Witkin, D. Terzopoulos, Snakes: active contour models, *Int. J. Comput. Vis.* 1 (4) (1987) 321–331.
- [2] R. Kimmel, A. Amir, A. Bruckstein, Finding shortest paths on surfaces using level set propagation, *IEEE Trans. Pattern Anal. Mach. Intell.* 17 (6) (1995) 635–640.
- [3] V. Caselles, R. Kimmel, G. Sapiro, Geodesic active contours, *Int. J. Comput. Vis.* 22 (1) (1997) 61–79.
- [4] R. Malladi, J.A. Sethian, B.C. Vemuri, Shape modeling with front propagation: a level set approach, *IEEE Trans. Pattern Anal. Mach. Intell.* 17 (2) (1995) 158–175.
- [5] C. Xu, J. Prince, Snakes, shapes, and gradient vector flow, *IEEE Trans. Image Process.* 7 (3) (1998) 359–369.
- [6] C. Xu, J. Prince, Generalized gradient vector flow external forces for active contours, *Signal Process.* 71 (2) (1998) 131–139.
- [7] C. Li, C. Xu, C. Gui, M.D. Fox, Level set evolution without re-initialization: a new variational formulation, in: *Proceedings of IEEE Conference on Computer Vision and Pattern Recognition (CVPR)*, vol. 1, 2005, pp. 430–436.
- [8] R. Ronfard, Region-based strategies for active contour models, *Int. J. Comput. Vis.* 13 (2) (1994) 229–251.
- [9] A. Yezzi, A. Tsai, A. Willsky, A statistical approach to snakes for bimodal and trimodal imagery, in: *Seventh IEEE International Conference on Computer Vision*, vol. 2, Washington, DC, USA, 1999, pp. 898–903.
- [10] C. Samson, L. Blanc-Feraud, G. Aubert, J. Zerubia, A variational model for image classification and restoration, *IEEE Trans. Pattern Anal. Mach. Intell.* 22 (5) (2000) 460–472.
- [11] T. Chan, L. Vese, Active contours without edges, *IEEE Trans. Image Process.* 10 (2) (2001) 266–277.
- [12] A. Tsai, A. Yezzi, A.S. Willsky, Curve evolution implementation of the Mumford–Shah functional for image segmentation, denoising, interpolation, and magnification, *IEEE Trans. Image Process.* 10 (8) (2001) 1169–1186.
- [13] N. Paragios, R. Deriche, Geodesic active regions and level set methods for supervised texture segmentation, *Int. J. Comput. Vis.* 46 (3) (2002) 223–247.



- [14] L. Vese, T. Chan, A multiphase level set framework for image segmentation using the Mumford and Shah model, *Int. J. Comput. Vis.* 50 (3) (2002) 271–293.
- [15] M. Rousson, R. Deriche, A variational framework for active and adaptative segmentation of vector valued images, in: *IEEE Workshop on Motion and Video Computing*, 2002, pp. 52–62.
- [16] J. Piovano, M. Rousson, T. Papadopoulos, Efficient segmentation of piecewise smooth images, in: *SSVM*, 2007, pp. 709–720.
- [17] C. Li, R. Huang, Z. Ding, C. Gatenby, D. Metaxas, J. Gore, A variational level set approach to segmentation and bias correction of medical images with intensity inhomogeneity, in: *Proceedings of Medical Image Computing and Computer Aided Intervention (MICCAI)*, Lecture Notes in Computer Science, vol. 5242, Part II, Springer, Berlin, 2008, pp. 1083–1091.
- [18] L. Wang, C. Li, Q. Sun, D. Xia, C. Kao, Brain MR image segmentation using local and global intensity fitting active contours/surfaces, in: *Proceedings of Medical Image Computing and Computer Aided Intervention (MICCAI)*, Lecture Notes in Computer Science, vol. 5241, Part I, Springer, Berlin, 2008, pp. 384–392.
- [19] A.K. Jain, Y. Zhong, M. Dubuisson-Jolly, Deformable template models: a review, *Signal Process.* 71 (2) (1998) 109–129.
- [20] D. Cremers, M. Rousson, R. Deriche, A review of statistical approaches to level set segmentation: integrating color, texture, motion and shape, *Int. J. Comput. Vis.* 72 (2) (2007) 195–215.
- [21] L. He, Z. Peng, B. Everding, X. Wang, C. Han, K. Weiss, W. Wee, A comparative study of deformable contour methods on medical image segmentation, *Image Vision Comput.* 26 (5) (2008) 141–163.
- [22] D. Mumford, J. Shah, Optimal approximations by piecewise smooth functions and associated variational problems, *Commun. Pure Appl. Math.* 42 (5) (1989) 577–685.
- [23] C. Li, C. Kao, J. Gore, Z. Ding, Implicit active contours driven by local binary fitting energy, in: *Proceedings of IEEE Conference on Computer Vision and Pattern Recognition (CVPR)*, IEEE Computer Society, Washington, DC, USA, 2007, pp. 1–7.
- [24] C. Xu, D. Pham, J. Prince, Image segmentation using deformable models, in: J. Fitzpatrick, M. Sonka (Eds.), *Handbook of Medical Imaging, Medical Image Processing and Analysis*, vol. 2, SPIE Press, 2000, pp. 129–174.
- [25] C. Li, Active contours with local binary fitting energy, in: *IMA Workshop on New Mathematics and Algorithms for 3-D Image Analysis*, 2006.
- [26] J. An, M. Rousson, C. Xu,  $\Gamma$ -convergence approximation to piecewise smooth medical image segmentation, in: *MICCAI* (2), 2007, pp. 495–502.
- [27] S. Lankton, D. Nain, A. Yezzi, A. Tannenbaum, Hybrid geodesic region-based curve evolutions for image segmentation, in: *SPIE Medical Imaging 2007 Symposium*, vol. 6510, 2007.
- [28] T. Brox, From pixels to regions: partial differential equations in image analysis, Ph.D. Thesis, Saarland University, Germany, 2005.
- [29] B. Rosenhahn, T. Brox, J. Weickert, Three-dimensional shape knowledge for joint image segmentation and pose tracking, *Int. J. Comput. Vis.* 73 (3) (2007) 242–262.
- [30] T. Brox, D. Cremers, On the statistical interpretation of the piecewise smooth Mumford–Shah functional, in: *SSVM07, Ischia, Italy*, 2007, pp. 203–213.
- [31] C. Li, C. Kao, J.C. Gore, Z. Ding, Minimization of region-scalable fitting energy for image segmentation, *IEEE Trans. Image Process.* 17 (10) (2008) 1940–1949.
- [32] S. Zhu, A. Yuille, Region competition: unifying snakes, region growing, and Bayes/MDL for multiband image segmentation, *IEEE Trans. Pattern Anal. Mach. Intell.* 18 (9) (1996) 884–900.
- [33] J. Kim, J. Fisher, A. Yezzi, M. Cetin, A. Willsky, Nonparametric methods for image segmentation using information theory and curve evolution, in: *IEEE International Conference on Image Processing*, vol. 3, 2002, pp. 797–800.
- [34] M. Rousson, T. Brox, R. Deriche, Active unsupervised texture segmentation on a diffusion based feature space, in: *IEEE Computer Society Conference on Computer Vision and Pattern Recognition*, 2003, pp. 699–704.
- [35] D. Comaniciu, P. Meer, Mean shift: a robust approach toward feature space analysis, *IEEE Trans. Pattern Anal. Mach. Intell.* 24 (5) (2002) 603–619.
- [36] C. Christoudias, B. Georgescu, P. Meer, Synergism in lowlevel vision, in: *16th International Conference on Pattern Recognition*, 2002, pp. 150–155.
- [37] G. Aubert, P. Kornprobst, *Mathematical Problems in Image Processing: Partial Differential Equations and the Calculus of Variations*, Springer, New York, 2002.